The structure of strong Indian monsoon low-pressure systems in Subseasonal-to-Seasonal prediction models

Article

Published Version

It is advisable to refer to the publisher's version if you intend to cite from the work. See [Guidance on citing](#).

RESEARCH ARTICLE

The structure of strong Indian monsoon low-pressure systems in subseasonal-to-seasonal prediction models

A. Deoras[1] | **A. G. Turner[1,2]** | **K. M. R. Hunt[1,2]**

[1]Department of Meteorology, University of Reading, Reading, UK

[2]National Centre for Atmospheric Science, University of Reading, Reading, UK

Correspondence
A. Deoras, Department of Meteorology, University of Reading, Reading, RG6 6EG, UK
Email: a.s.deoras@pgr.reading.ac.uk

Abstract

The structure of strong Indian monsoon low-pressure systems (LPSs) up to forecast lead times of 15 days in 11 models of the Subseasonal-to-Seasonal (S2S) Prediction Project is analysed. Strong LPS (SLPS) tracks are obtained from a catalogue of LPSs tracked in all ensemble members of the S2S models during a common reforecast period of June–September 1999–2010. SLPSs, which have a minimum intensity equal to at least the upper-quartile intensity of all LPSs, are then composited to generate horizontal and vertical structures of several dynamic and thermodynamic fields. The evolution of fields with forecast lead time and during LPS lifecycle is analysed. Furthermore, the simulation of the lower-tropospheric monsoon circulation, precipitation biases, and the precipitation contribution of LPSs are analysed. All S2S models and the multimodel mean simulate the lower-tropospheric monsoon circulation, but prominent dry biases are observed in the Australian Bureau of Meteorology and Environment and Climate Change Canada models. The precipitation contribution of LPSs to the summer mean precipitation is smaller in all S2S models than in tracks derived from ERA-Interim reanalysis. The location and amplitude of the lower-tropospheric cold core and the location of maximum precipitation are not well simulated by many models, particularly by the Hydrometeorological Centre of Russia model, in which the cold core is missing altogether. The structure of relative vorticity anomaly in all S2S models and the multimodel mean is shallower and weaker than in ERA-Interim and MERRA-2 reanalyses. Though the cold core intensifies through the LPS lifecycle in all models, the warm core features a midlife maximum, except in models such as Australian Bureau of Meteorology and China Meteorological Administration. These results demonstrate the potential for S2S models at simulating the structure of SLPSs, benefiting stakeholders that use S2S models for forecasting.

KEYWORDS

Indian monsoon, Indian monsoon low-pressure systems, monsoon depressions, S2S

Abbreviations: SLPS, Strong Indian monsoon low-pressure systems; S2S, Subseasonal-to-Seasonal

1 | INTRODUCTION

Indian monsoon low-pressure systems (LPSs) are synoptic-scale cyclonic vortices that typically develop in the quasi-stationary monsoon trough before propagating westnorthwestward during the summer monsoon season (June–September) and have a typical lifespan of 3–5 days (Mooley, 1973; Godbole, 1977; Sikka, 1978; Saha *et al.*, 1981; Hunt and Parker, 2016). These systems are an important component of the Indian monsoon since they produce around 50% of the summer monsoon precipitation over India (Yoon and Chen, 2005; Hunt and Fletcher, 2019) and up to 70% of the summer monsoon precipitation over the east coast (Deoras *et al.*, 2021b), benefiting Indian society dependent on rain fed agriculture for their livelihood. Though LPSs enable the recharge of groundwater, strong LPSs (SLPSs) often trigger catastrophic floods in the Indian subcontinent (e.g., Hunt and Menon, 2020), causing adverse socio-economic impacts.

The India Meteorological Department classifies LPSs on the basis of their mean sea-level pressure anomaly or surface wind speeds (http://imdnagpur.gov.in/docs_general/monsoonfaq.pdf). The systems featuring two closed isobars in surface pressure at 2 hPa intervals over land, or those featuring 3-min maximum sustained surface wind speeds of 8.5–13 m·s^{-1} over sea, are referred to as monsoon depressions (MDs), whereas systems weaker than this are referred to as monsoon low-pressure areas. Typically, around 14 LPSs form each summer, of which two to six intensify into SLPSs, such as MDs (Sarker and Chowdhury, 1988; Boos *et al.*, 2015; Hunt *et al.*, 2016a). Though SLPSs such as MDs mostly form over the head of the Bay of Bengal (BoB) and nearby coastal regions, other regional LPS varieties can form over the Arabian Sea and around Sri Lanka (Deoras *et al.*, 2021b).

The occurrence of LPSs was reported as early as the late 19th century by Eliot (1884), who found that LPSs regularly form during July and August, they are weaker than tropical cyclones, and most of them dissipate without reaching northwestern parts of India. In the 20th century, many studies analysed synoptic features of MDs. Mulky and Banerji (1960) analysed circulation features of a composite of 22 MDs that occurred between 1954 and 1958. They found that MDs are zonally asymmetric with a tilt towards the southwest, a feature previously reported by Pisharoty and Asnani (1957), and later reconfirmed by Mooley (1973) in a larger composite of MDs occurring during 1891–1960. Using meteorological charts and radiosonde data, Krishnamurti et al. (1975, 1976), Godbole (1977), and Sarker and Chowdhury (1988) analysed more fields associated with MDs, such as temperature and relative vorticity. They found that MDs have a cold (warm) core in the lower (upper) troposphere, with the most intense relative vorticity, winds, moisture, cloud cover, and precipitation occurring in the southwestern quadrant of the composite MD.

Though LPS studies in the last century were constrained by the lack of observations, especially over the BoB, the availability of extensive satellite and reanalysis datasets in this century has facilitated the investigation of more properties of LPSs. Hurley and Boos (2015), who developed a global climatology of monsoon LPSs, found that the thermal structure of MDs over India is similar to those over the western Pacific and northern Australia. Hunt *et al.* (2016a) performed a composite analysis of 106 MDs that occurred between 1979 and 2014. Apart from confirming the previously known features of MDs, they found that MDs occurring during active phases of the monsoon are more intense than those during break phases. Most recently, Deoras *et al.* (2021b) analysed the thermal and moisture structures of a composite of 505 LPSs occurring between 1979 and 2018, which were partitioned into four regional varieties. We found that whilst all four varieties feature a similar structure, there was a significant basin-dependent variability in the moist thermodynamics.

Given the important role of LPSs during the summer monsoon season, it is necessary to understand the skill of LPS predictions, especially on an extended time scale of 15 days that is important for disaster preparedness and informing agricultural practice. Deoras *et al.* (2021a) investigated the prediction skill of LPSs in 11 models of the Subseasonal-to-Seasonal (S2S) Prediction Project (Vitart *et al.*, 2017) during June–September 1999–2010. They found that S2S models are able to simulate LPSs in general, but large biases are observed in the Australian Bureau of Meteorology (BoM), China Meteorological Administration (CMA), and Hydrometeorological Centre of Russia (HMCR) models. In fact, the multimodel mean (MMM) track forecast error for LPSs at lead times of 4 days is approximately twice that of the India Meteorological Department's long-period average track error for tropical cyclones over the north Indian Ocean (Mishra *et al.*, 2021). Therefore, it is important to improve the skill of LPS forecasts, for which it is essential to understand how S2S models simulate the structure and behaviour of LPSs. In this article, we focus on SLPSs due to their impacts on the Indian subcontinent during the summer monsoon season; our aim is to understand the following aspects:

- How well do S2S models simulate the circulation and summer mean precipitation?
- How well do S2S models simulate the structure of SLPSs?

- How do fields associated with LPSs evolve with forecast lead time and through LPS lifetime in S2S models?

We present an outline of the data and methodology in Section 2. We look at the simulation of the lower-tropospheric South Asian monsoon circulation in Section 3, and precipitation biases and the precipitation contribution of LPSs in Section 4. We then investigate the storm-centred horizontal and vertical structures of LPSs in Sections 5 and 6, respectively, and evolution of fields in Section 7. We finally conclude in Section 8.

2 | DATA AND METHODS

2.1 | S2S database

The S2S database consists of reforecasts from the following 11 meteorological centres: the BoM, CMA, Environment and Climate Change Canada (ECCC), European Centre for Medium-Range Weather Forecasts (ECMWF), HMCR, Institute of Atmospheric Sciences and Climate of the National Research Council (ISAC-CNR), Japan Meteorological Agency (JMA), Korea Meteorological Administration (KMA), Météo-France/Centre National de Recherche Meteorologiques (CNRM), National Centers for Environmental Prediction (NCEP), and UK Met Office (UKMO). Table 1 shows details of the configuration of S2S reforecasts. Each reforecast comprises a control reforecast as well as perturbed reforecasts that produce ensemble members. BoM reforecasts are archived on a $2.5° × 2.5°$ grid, whereas other S2S models are archived on a $1.5° × 1.5°$ grid. All reforecasts are archived at a daily resolution. Despite differences in the reforecast configuration (e.g., reforecast frequency), there are enough commonalities in the 11 S2S models to make intercomparisons (Vitart et al., 2017). Following previous studies using the S2S dataset (e.g., Jie et al., 2017; Vitart, 2017; Lee et al., 2018), we assume that any bias in our results due to heterogeneity in the reforecast configuration will be insignificant. Since all S2S models cover a common reforecast period of 1999–2010, we consider reforecasts starting between May and September 1999–2010 in this work. For tracking LPSs (see Section 2.1), we use mean sea-level pressure, u and v winds at 850 hPa and temperature at 925 hPa; these variables are instantaneous (0000 UTC). We use the same model versions considered by Deoras et al. (2021a) for consistency. For analysing vertical structure, we use all available pressure levels in the archive, which are 1,000, 925, 850, 700, 500, 300, 200, and 100 hPa. We compute anomalies against the summer mean climatology in all S2S models and reanalysis datasets (to be discussed in Section 2.2). For S2S models, we consider the reforecast

period between June 1 and September 30, 1999–2010, in all reforecasts starting between May 1 and September 30, provided this period is within the first 15 days of each reforecast.

2.2 | LPS database

We use a catalogue of LPSs (Deoras et al., 2021c) tracked in all ensemble members of 11 S2S models, ECMWF ERA-Interim (ERA-I) reanalysis and Modern-Era Retrospective Analysis for Research and Applications, version 2 (MERRA-2). The details of this dataset are described in Deoras et al. (2021a). In this catalogue, LPSs, which include monsoon low-pressure areas, MDs, and deep depressions, were tracked using a feature-tracking algorithm (Hunt et al., 2016a; 2018) based on 850 hPa relative vorticity. Since LPSs feature a warm-over-cold core structure (e.g., Godbole, 1977), non-LPSs were filtered out from potential LPSs using a temperature–pressure filter—a track is removed from the dataset if all of its track points have 925 hPa temperature anomalies greater than or equal to 0.5 K or non-negative mean sea-level pressure anomalies at the centre. The climatologies of 925 hPa temperature and mean sea-level pressure for track filtering were computed by averaging all reforecasts starting the same day and the same month, but excluding the actual year of reforecasts, following which the forecast anomalies were calculated by subtracting climatologies from the ensemble member. Only those LPSs featuring lysis within the first 15 days of reforecasts were retained for further analysis. Here, we define SLPSs as systems whose minimum intensity (central 850 hPa relative vorticity) reaches at least the 75th percentile of the population of all tracked LPSs in the respective S2S model or reanalysis dataset. Intensity thresholds are given in Table 1.

2.3 | Reanalysis datasets

We verify the results of S2S models against ERA-I (Dee et al., 2011) and MERRA-2 (Gelaro et al., 2017) reanalysis datasets. ERA-I is available at a spatial resolution of $\sim 0.7° × 0.7°$ and a temporal resolution of 6 hr, whereas MERRA-2 has a spatial resolution of $0.625° × 0.5°$ (longitude × latitude) and a temporal resolution of 3 hr. For analysing the vertical structure of LPSs in these datasets, we use the same model output levels discussed in Section 2.1. We verify the results against the MERRA-2 dataset to account for observational uncertainty. We compute forecast anomalies against a summer mean climatology (June–September 1999–2010) for ERA-I and MERRA-2 reanalysis datasets.

TABLE 1 Configuration of reforecasts in 11 subseasonal-to-seasonal models and ERA-Interim and MERRA-2 reanalysis datasets used in this article

Model	Resolution	Ensemble size	Reforecast frequency	Intensity threshold
BoM	$\sim 2.00° \times 2.00°$, L17	33	Six per month	6.16
CMA	$\sim 1.00° \times 1.00°$, L40	4	Daily	4.97
CNRM	$\sim 0.70° \times 0.70°$, L91	15	Four per month	3.80
ECCC	$0.45° \times 0.45°$, L40	4	Weekly	3.99
ECMWF	$0.25° \times 0.25°$, L91	11	Two per week	4.16
HMCR	$1.10° \times 1.40°$, L28	10	Weekly	2.97
ISAC-CNR	$0.80° \times 0.56°$, L54	5	Every 5 days	4.43
JMA	$\sim 0.50° \times 0.50°$, L100	5	Three per month	3.92
KMA	$\sim 0.50° \times 0.50°$, L85	3	Four per month	4.31
NCEP	$\sim 1.00° \times 1.00°$, L64	4	Daily	4.17
UKMO	$\sim 0.50° \times 0.80°$, L85	7	Four per month	4.35
ERA-Interim	$\sim 0.70° \times 0.70°$, L60	—	—	3.97
MERRA-2	$\sim 0.63° \times 0.50°$, L72	—	—	5.11

Note: The intensity threshold column shows the minimum intensity of strong Indian monsoon low-pressure systems, which is based on the upper-quartile values of central 850 hPa relative vorticity of low-pressure systems in each model, ERA-Interim, and MERRA-2.

Abbreviations: BoM, Australian Bureau of Meteorology; CMA, China Meteorological Administration; ECCC, Environment and Climate Change Canada; ECMWF, European Centre for Medium-Range Weather Forecasts; HMCR, Hydrometeorological Centre of Russia; ISAC-CNR, Institute of Atmospheric Sciences and Climate of the National Research Council; JMA, Japan Meteorological Agency; KMA, Korea Meteorological Administration; CNRM, Météo-France/Centre National de Recherche Meteorologiques; NCEP, National Centers for Environmental Prediction; UKMO, UK Met Office; MERRA-2, Modern-Era Retrospective Analysis for Research and Applications, version 2.

2.4 | Global Precipitation Measurement Integrated Multisatellite Retrievals for GPM

We use the Global Precipitation Measurement (GPM) Integrated Multisatellite Retrievals for GPM (IMERG) dataset (Huffman *et al.*, 2015) for evaluating precipitation biases in S2S models. We also use this dataset to determine the precipitation contribution and the horizontal structure of precipitation of LPSs tracked in the ERA-I and MERRA-2 datasets. GPM IMERG is a merged precipitation product that provides precipitation estimates on a $0.1° \times 0.1°$ grid globally every 0.5 hr. It shows notable improvements over other precipitation products, such as the Tropical Rainfall Measuring Mission Multisatellite Precipitation Analysis in capturing heavy rainfall over India during the summer monsoon season, and represents mean-monsoon rainfall more realistically (Prakash *et al.*, 2016; 2018; Liu 2016). However, it has difficulty at detecting rainfall over northeastern and southeastern parts of India. Furthermore, it underestimates the frequency of heavy rainfall over northeastern parts of India due to the orography (Prakash *et al.*, 2018). For most analysis in this study, we regrid the IMERG dataset to a spatial resolution of $1° \times 1°$ for a fair comparison with the coarser S2S dataset, similar to Deoras *et al.* (2021a).

2.5 | Significance testing and root-mean-square error

We perform an independent *t*-test (Snedecor and Cochran, 1989) for each S2S model and MERRA-2 to determine if their composite states significantly differ from ERA-I. Our null hypothesis states that an LPS composite in an S2S model or MERRA-2 has identical average values to the composite in ERA-I. Areas where the 95% significance level is not satisfied will be stippled, and red line contours will be shown in corresponding figures. Furthermore, in order to compare the S2S results with ERA-I and MERRA-2, we calculate a root-mean-square error for different fields over the plotting domain. For vertical composites, the root-mean-square error value in a model output level is weighted by the density of air in that level. This will facilitate a comparison of our results with future studies that might consider vertical levels different from those here.

3 | SIMULATION OF THE LOWER-TROPOSPHERIC SOUTH ASIAN MONSOON CIRCULATION

In this section, we first investigate the simulation of the mean state of the lower-tropospheric South Asian

monsoon circulation (hereafter referred to as the monsoon circulation), and then investigate its simulation on SLPS days (i.e., when at least one SLPS was present in the domain). We consider forecast lead times of 0–15 days in all ensemble members of 11 S2S models. Jie *et al.* (2017) investigated biases in the simulation of the monsoon circulation in control forecasts of 10 S2S models at forecast lead times of 10 days; however, their analysis was limited to the transition (May 25–June 25) and mature (June 25–July 25) phases of the Indian monsoon. We remain, therefore, without a complete understanding of the simulation of the monsoon circulation by S2S models at lead times of up to 15 days during the climatological period as well as on SLPS days.

Figure 1 shows the climatology of 850 hPa winds in 11 S2S models at lead times of up to 15 days, ERA-I and MERRA-2 during June–September 1999–2010. The MMM

of S2S models is also shown. All S2S models and the MMM are able to simulate the main features of the monsoon circulation, such as the cross-equatorial flow, Somali Jet, and the position of the monsoon trough, and most models have a root-mean-square error consistent with the observational uncertainty. The monsoon trough, however, is located further to the south in the BoM model than in others. As a result, there are strong westerly winds over most of the Arabian Sea, southern India, and very weak northwesterly winds over north-central and northern parts of India. The BoM model has the largest root-mean-square error in wind speed, and the spread of errors in S2S models is larger than the observational uncertainty (i.e., the root-mean-square error between MERRA-2 and ERA-I). We now turn to 850 hPa wind anomalies (Figure 2), which are computed by subtracting the summer mean climatology from 850 hPa winds on SLPS days. The summer mean
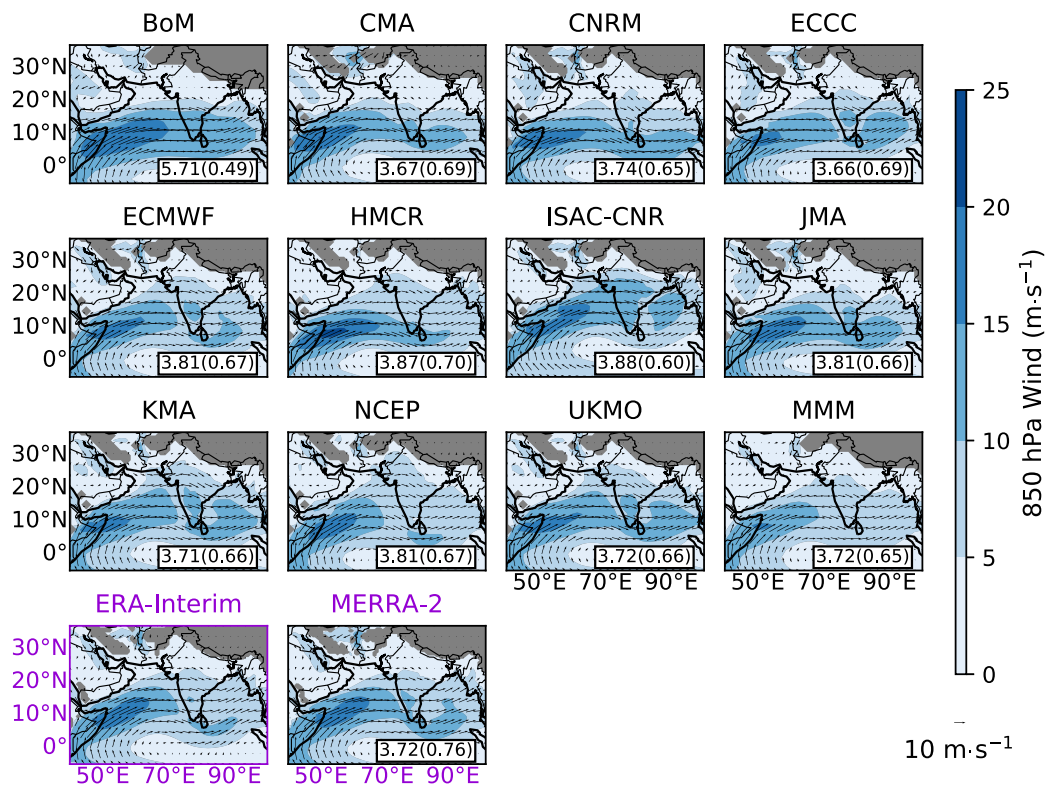

FIGURE 1 Contours show the climatology of 850 hPa winds (m·s⁻¹) in all ensemble members of 11 subseasonal-to-seasonal (S2S) models and ERA-Interim and Modern-Era Retrospective Analysis for Research and Applications, version 2 (MERRA-2) reanalysis datasets during June–September 1999–2010. The multimodel mean (MMM) of S2S models is also shown. The climatology is considered for forecast lead times of 0–15 days in all S2S models and the MMM. Wind vectors in each subplot are regridded to match the coarsest spatial resolution of the BoM model, which is 2.5° × 2.5°. Numbers outside parentheses in each subplot indicate the root-mean-square error in the wind speed (m·s⁻¹) between the respective S2S models and ERA-Interim, whereas those in parentheses indicate the pattern correlation coefficient between the respective S2S models and ERA-Interim. BoM, Australian Bureau of Meteorology; CMA, China Meteorological Administration; ECCC, Environment and Climate Change Canada; ECMWF, European Centre for Medium-Range Weather Forecasts; HMCR, Hydrometeorological Centre of Russia; ISAC-CNR, Institute of Atmospheric Sciences and Climate of the National Research Council; JMA, Japan Meteorological Agency; KMA, Korea Meteorological Administration; CNRM, Météo-France/Centre National de Recherche Meteorologiques; NCEP, National Centers for Environmental Prediction; UKMO, UK Met Office [Colour figure can be viewed at wileyonlinelibrary.com]
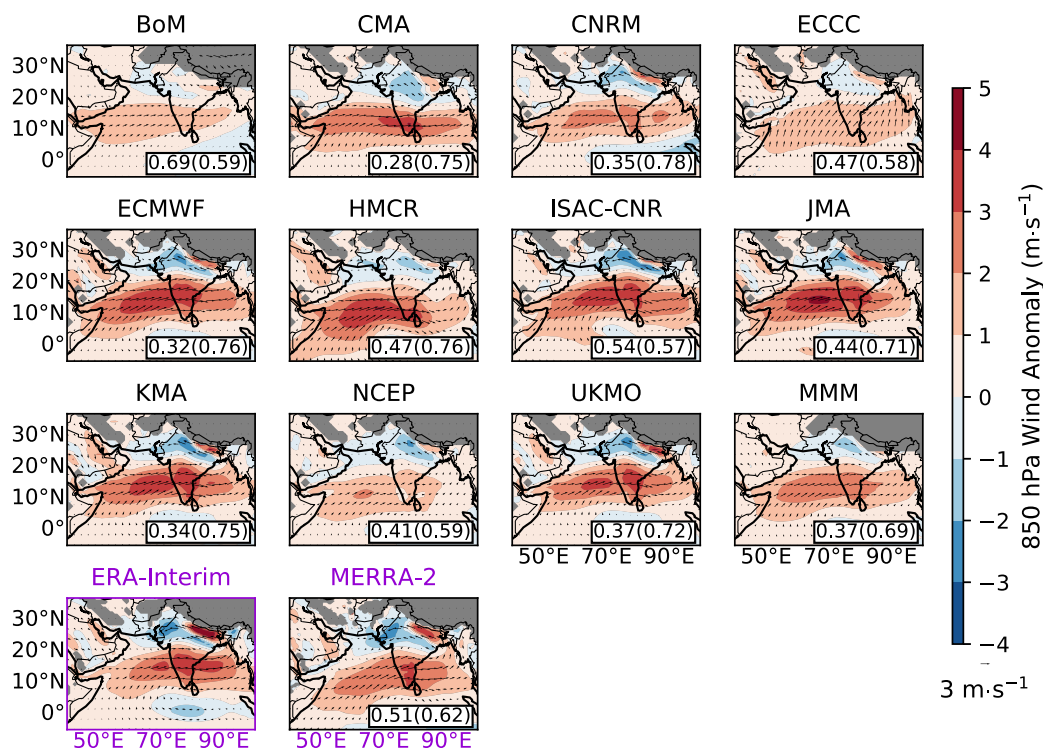
FIGURE 2 As Figure 1, but for wind anomaly on strong Indian monsoon low-pressure system days. Contours show the wind anomaly, which is computed against the summer mean climatology for subseasonal-to-seasonal models, the multimodel mean (MMM), ERA-Interim, and Modern-Era Retrospective Analysis for Research and Applications, version 2 (MERRA-2). BoM, Australian Bureau of Meteorology; CMA, China Meteorological Administration; ECCC, Environment and Climate Change Canada; ECMWF, European Centre for Medium-Range Weather Forecasts; HMCR, Hydrometeorological Centre of Russia; ISAC-CNR, Institute of Atmospheric Sciences and Climate of the National Research Council; JMA, Japan Meteorological Agency; KMA, Korea Meteorological Administration; CNRM, Météo-France/Centre National de Recherche Meteorologiques; NCEP, National Centers for Environmental Prediction; UKMO, UK Met Office [Colour figure can be viewed at wileyonlinelibrary.com]

climatology (June–September 1999–2010) is computed for forecast lead times of 0–15 days in all ensemble members of each S2S model. The cross-equatorial monsoon flow strengthens on SLPS days in all S2S models, the MMM, ERA-I, and MERRA-2, evidenced by positive anomalies over the Arabian Sea, southern India, and the BoB. This suggests that SLPSs influence the simulation of the monsoon circulation. The wind anomaly is smallest in the BoM and ECCC models. Furthermore, winds are inaccurately simulated by the ECCC model since there are anomalous southwesterly winds over the Arabian Sea at 15°N and anomalous southerly winds over the BoB at 10°N instead of westerlies. However, the root-mean-square error for most models is smaller than the observational uncertainty. As with the climatology, the root-mean-square error is largest in the BoM model with respect to ERA-I and smallest in the CMA model with respect to both ERA-I and MERRA-2.

In summary, S2S models and the MMM well simulate the monsoon circulation during the climatological period and on SLPS days in general. Models such as CMA, ECMWF, KMA, and UKMO have the best performance, whereas BoM and ECCC have prominent biases.

4 | PRECIPITATION

In this section, we investigate precipitation biases and the precipitation contribution of LPSs to the modelled summer mean precipitation. We carry out these analyses for forecast lead times of 0–15 days during June–September 2001–2010. These results could help stakeholders in many ways. The modelling community could thoroughly investigate reasons for precipitation biases, which would be useful for improving S2S precipitation forecasts in the future. Models featuring small biases in forecasts of precipitation as well as the precipitation contribution of LPSs can be used for developing better forecast products, thereby favouring better management of water resources. Since individual LPS events can cause significant floods in the Indian subcontinent, meteorologists and hydrologists can use such models for LPS forecasting, resulting in improved flood preparedness and agricultural decision making. Here
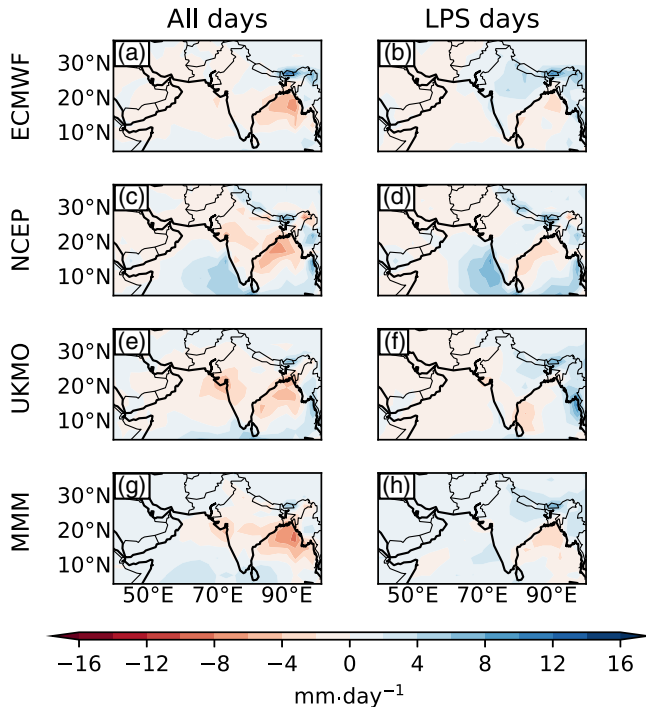
FIGURE 3 Precipitation bias (mm·day⁻¹) in the (a, b) European Centre for Medium-Range Weather Forecasts (ECMWF), (c, d) National Centers for Environmental Prediction (NCEP), (e, f) UK Met Office (UKMO) models, and (g, h) the multimodel mean (MMM) of the 11 subseasonal-to-seasonal models for forecast lead times of 0–15 days during June–September 2001–2010. For each model, the bias is calculated as the model precipitation minus Global Precipitation Measurement (GPM) Integrated Multisatellite Retrievals for GPM precipitation for all days (left column) and low-pressure system (LPS) days (right column) [Colour figure can be viewed at wileyonlinelibrary.com]

we consider LPSs instead of SLPSs since weaker LPSs (e.g., low-pressure areas) still provide a significant precipitation contribution to the summer mean precipitation (Hunt and Fletcher, 2019).

4.1 | Precipitation biases

Figure 3 shows precipitation biases for all ensemble members of the three best-performing models: ECMWF, NCEP, and UKMO. The result for the MMM is also shown in Figure 3, whereas the results for other models are shown in Figure S1. The biases are calculated for all days (i.e., climatology) and LPS days (i.e., when at least one LPS was present in the domain). Since the BoM model has the coarsest resolution (2.5° × 2.5°), precipitation datasets of other S2S models and IMERG are regridded to this resolution. The biases are then calculated by subtracting IMERG precipitation from each model.

In all models, the patterns of precipitation biases on all days are similar to those on LPS days, suggesting that LPSs are among the important contributors to precipitation biases. In the BoM and CMA models, there are prominent dry biases over the monsoon core zone (Rajeevan *et al.*, 2010), northeastern India, BoB, and nearby coastal regions on all days and LPS days. Whereas the CNRM, HMCR, ISAC-CNR, and NCEP models simulate weak dry biases over the monsoon core zone on all days, the ECCC and JMA models simulate weak wet biases. In contrast, the ISAC-CNR model simulates strong wet biases along the Himalayan foothills and parts of eastern India on all days. In all models, LPSs reduce dry precipitation biases over the head of the BoB and the monsoon core zone, whereas in the ECCC model they increase the wet bias. This is because LPSs usually inhabit these regions. The MMM features small dry biases over the BoB and small wet biases over India on all days. The pattern is reversed on LPS days.

The dry biases over the monsoon core zone, head of the BoB, and nearby coastal regions are well known in the current general circulation models, including the MMM of CMIP5 and CMIP3 models (e.g., Sperber *et al.*, 2013; Praveen *et al.*, 2015). Here, following Sperber *et al.* (2013) and Jie *et al.* (2017), we investigate how precipitation biases are associated with biases in the lower-tropospheric monsoon circulation. Figure S2 shows biases in 850 hPa winds on all days computed against ERA-I. These results are considered for forecast lead times of 0–15 days. The overall biases in the MMM are smaller than those in individual S2S models. The BoM, CMA, and CNRM models have strong easterly or northeasterly anomalies over the head of the BoB and the monsoon core zone, suggesting that dry precipitation biases are associated with a weak monsoon flow. This is also seen in models such as JMA and NCEP, in which prominent dry biases over the Myanmar coast are associated with easterly wind anomalies. In contrast, a prominent wet bias over the monsoon trough region in the ECCC model and wet biases along the Himalayan foothills in the ISAC-CNR model are associated with strong westerly wind anomalies. These results agree with Jie *et al.* (2017) in general, who found similar wind biases at forecast lead times of 10 days in control runs of 10 S2S models. We will explore the precipitation contribution of LPSs in the next subsection to better understand these results.

4.2 | Precipitation contribution

Figure 4 shows the precipitation contribution of LPSs to the summer mean precipitation in all ensemble members as well as the MMM of 11 S2S models. The results for LPSs tracked in ERA-I and MERRA-2, for which GPM IMERG precipitation is used, are also shown. We attribute
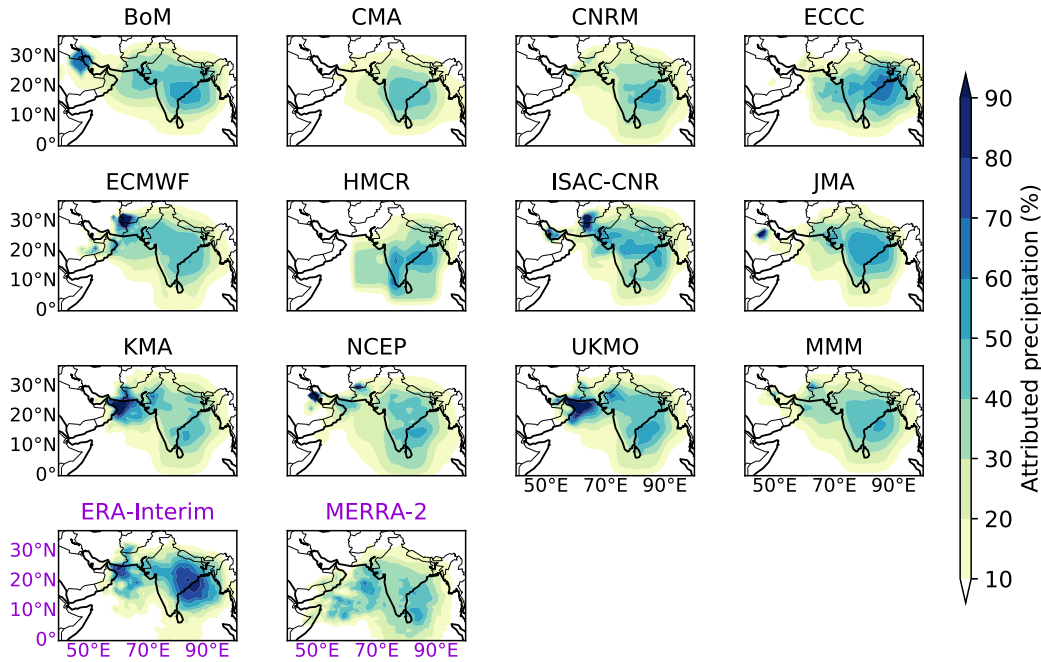
FIGURE 4 Percentage of seasonal (June–September 2001–2010) precipitation attributed to monsoon low-pressure systems tracked in all ensemble members of 11 subseasonal-to-seasonal (S2S) models for forecast lead times of 0–15 days and ERA-Interim and MERRA-2 reanalysis datasets. Precipitation is attributed to a low-pressure system if it falls within 800 km of its centre. The multimodel mean (MMM) of S2S models is also shown, which is computed by regridding the precipitation contribution in each S2S model to the coarsest spatial resolution of the BoM model (2.5° × 2.5°). The Global Precipitation Measurement (GPM) Integrated Multisatellite Retrievals for GPM dataset is used for calculating the precipitation contribution of monsoon low-pressure systems tracked in ERA-Interim and MERRA-2 reanalysis datasets. The subplots of ERA-Interim and MERRA-2 are highlighted in dark violet to distinguish them from the S2S dataset. BoM, Australian Bureau of Meteorology; CMA, China Meteorological Administration; ECCC, Environment and Climate Change Canada; ECMWF, European Centre for Medium-Range Weather Forecasts; HMCR, Hydrometeorological Centre of Russia; ISAC-CNR, Institute of Atmospheric Sciences and Climate of the National Research Council; JMA, Japan Meteorological Agency; KMA, Korea Meteorological Administration; CNRM, Météo-France/Centre National de Recherche Meteorologiques; NCEP, National Centers for Environmental Prediction; UKMO, UK Met Office; MERRA-2, Modern-Era Retrospective Analysis for Research and Applications, version 2 [Colour figure can be viewed at wileyonlinelibrary.com]

precipitation to an LPS if it falls within 800 km of its centre, as initially suggested by Hunt and Fletcher (2019). The results agree with past studies (e.g., Hurley and Boos 2015; Hunt and Fletcher 2019; Deoras *et al.*, 2021b) in general—LPSs in most models and the MMM have the largest precipitation contribution over parts of eastern and east-central India and adjoining parts of the BoB. However, the precipitation contribution over eastern India is smaller in all S2S models than in ERA-I. Deoras *et al.* (2021a) found that all S2S models underestimate the frequency of LPSs. It is important, therefore, to delineate the roles of biases on LPS precipitation and LPS frequency in total LPS precipitation biases, for which we follow a linearised budget method. For each S2S model, we first approximate the total simulated precipitation (TP) as follows:

$$TP = P \times N, \qquad (1)$$

where P is the composite-mean LPS precipitation within 800 km of the LPS centre and N is the total number of LPSs.

From the results of ERA-I, we then apply bias corrections to P and N:

$$TP_{bc} = (P + P_b) \times (N + N_b), \qquad (2)$$

where TP_{bc} is the bias-corrected total precipitation, P_b is the precipitation bias, and N_b is the LPS frequency bias. We then determine the bias in the total simulated precipitation (TP_b) by subtracting Equation (1) from Equation (2) and ignoring the product term of P_b and N_b, which we assume to be small:

$$TP_b = (P \times N_b) + (N \times P_b). \qquad (3)$$

We then estimate relative contributions of frequency and precipitation biases to the total precipitation bias from Equation (3). Compared with LPS frequency biases, LPS precipitation biases in most models have a greater relative contribution (0.6–0.8) to the total precipitation bias over eastern India. In contrast, biases in LPS frequency in the

BoM, ECCC, and JMA models contribute the most (relative contribution exceeding 0.8) to the total precipitation bias over eastern India.

The precipitation contribution depends on the propagation of LPSs over India. We find that biases in the simulation of LPS tracks (e.g., see Deoras *et al.*, 2021a, figure 4) modulate their precipitation contribution. The precipitation contribution of LPSs in models such as the CMA and HMCR is the largest over south-central India since LPSs propagate further southward in these models than in others. In the ECMWF, ISAC-CNR, KMA, and UKMO models, there is a large precipitation contribution over northern parts of the Arabian Sea, as well as parts of Pakistan, Afghanistan, and Iran, which is attributed to long-lived BoB LPSs and Arabian LPSs, as suggested by Deoras *et al.* (2021b). The climatological precipitation over these regions during the summer monsoon season is very small, which means that any passing LPS makes a proportionately large contribution to precipitation. The precipitation contribution over the Arabian Sea is larger in MERRA-2 than in ERA-I, which is due to a larger frequency of Arabian LPSs (Deoras *et al.*, 2021a). Furthermore, the precipitation contribution of LPSs over eastern parts of India is smaller in MERRA-2 than in ERA-I, which is attributed to a lower track density.

In conclusion, stakeholders could benefit from precipitation forecasts from the MMM since precipitation biases are small and the MMM simulates the precipitation contribution reasonably well. They could also benefit from precipitation forecasts of the ECCC, ECMWF, ISAC-CNR, JMA, and UKMO models after applying suitable bias corrections.

5 | HORIZONTAL STRUCTURE OF SLPS

In this section, we discuss the horizontal structure of precipitation, 850 hPa wind, mean sea-level pressure and 850 hPa relative vorticity for composites of SLPSs. For compositing, we centralise each SLPS at each time step to 0° relative latitude and 0° relative longitude. We have not rotated composites in this study. Hunt *et al.* (2016b) compared unrotated and rotated composites of storm-centred precipitation for MDs. They found that the location of maximum precipitation, which is not collocated with the LPS centre, is not affected by rotation, whereas its magnitude is reduced in the rotated composite. Other fields (e.g., relative vorticity) feature smaller variance than precipitation, and their maxima are collocated with the LPS centre.

5.1 | Precipitation and wind

Figure 5 shows storm-centred precipitation for composites of SLPSs tracked in all ensemble members of eleven S2S models, the MMM, ERA-I and MERRA-2 during June–September 2001–2010. Vectors showing 850 hPa wind as an anomaly to the summer mean climatology are overlaid. The overall composite-mean precipitation produced by SLPSs in S2S models and the MMM is in agreement with that produced by observed MDs, as investigated in past studies (e.g., Stano *et al.* 2002). Whilst all models underestimate the maximum precipitation (considered within 800 km of the composite centre), there is a prominent underestimation in the maximum and composite-mean precipitation in the HMCR model, which also poorly simulates the 850 hPa wind anomaly. The MMM also underestimates the maximum and composite-mean precipitation. The BoM (CMA) model features the smallest (largest) root-mean-square error with respect to ERA-I. The error in S2S models is larger than the observational uncertainty in the composite-mean precipitation in reanalyses, which is calculated using the GPM IMERG dataset.

The region of maximum precipitation is located ∼ 300 km from the centre. In the CNRM, ECMWF, JMA, NCEP, and UKMO models, it is located to the southwest of the centre, which is in agreement with ERA-I, MERRA-2, and past studies (e.g., Godbole, 1977; Yoon and Chen 2005; Hunt *et al.* 2016a). In contrast, it is located to the relative south of the centre in the BoM, CMA, ECCC, HMCR, and ISAC-CNR models and the MMM. The region of maximum precipitation is located to the westsouthwest of the LPS centre, which is attributed to quasigeostrophic dynamical lifting (e.g., Sanders, 1984; Boos *et al.* 2015) and horizontal moisture advection (e.g., Adames and Ming 2018), with adiabatic quasigeostrophic ascent dominating in the lower troposphere over the maximum precipitation region (Rajamani and Rao, 1981; Murthy and Boos, 2020). We investigate moisture-flux convergence at 850 hPa (Figure S3), since other fields, such as vertical velocity, are not commonly available in S2S models. It should be noted that we have excluded the ISAC-CNR and KMA models, since specific humidity is not available. Among all S2S models, the HMCR model features the weakest moisture-flux convergence, which explains the lowest precipitation in this model. There is a strong positive linear correlation (Figure S6a) between mean moisture-flux convergence and mean precipitation (both considered within 800 km of the composite centre) among S2S models—the Pearson correlation coefficient is 0.84 and it is statistically significant at the 95% confidence level. Since LPSs are located closer to the Himalayas in BoM than
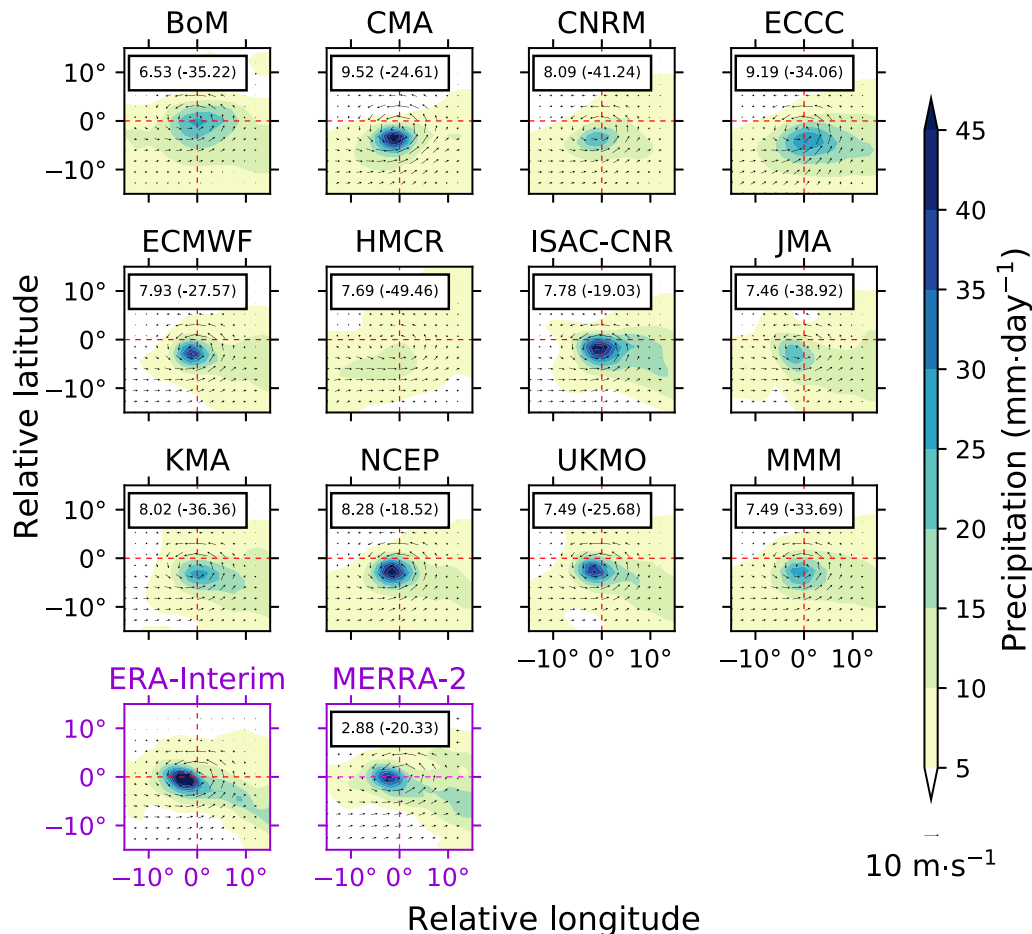
FIGURE 5 Storm-centred precipitation (mm·day^{-1}) for composites of strong Indian monsoon low-pressure systems (SLPSs) tracked in all ensemble members of 11 subseasonal-to-seasonal (S2S) models and ERA-Interim and Modern-Era Retrospective Analysis for Research and Applications, version 2 (MERRA-2) reanalysis datasets during June–September 2001–2010 (contours). Wind vectors showing the 850 hPa wind speed as an anomaly to the summer mean climatology for the same period are overlaid. These results are considered for forecast lead times of 0–15 days. The multimodel mean (MMM) of S2S models is also shown. The Global Precipitation Measurement (GPM) Integrated Multisatellite Retrievals for GPM (IMERG) dataset is used for calculating precipitation for SLPSs tracked in ERA-Interim. Numbers indicate the root-mean-square error in the composite-mean precipitation (mm·day^{-1}) between the respective S2S models and GPM IMERG for SLPSs in ERA-Interim, whereas numbers in parentheses indicate the error (mm·day^{-1}) in the maximum precipitation (within 800 km from the centre). For MERRA-2, numbers show the aforementioned errors between SLPSs in MERRA-2 and ERA-Interim. BoM, Australian Bureau of Meteorology; CMA, China Meteorological Administration; ECCC, Environment and Climate Change Canada; ECMWF, European Centre for Medium-Range Weather Forecasts; HMCR, Hydrometeorological Centre of Russia; ISAC-CNR, Institute of Atmospheric Sciences and Climate of the National Research Council; JMA, Japan Meteorological Agency; KMA, Korea Meteorological Administration; CNRM, Météo-France/Centre National de Recherche Meteorologiques; NCEP, National Centers for Environmental Prediction; UKMO, UK Met Office [Colour figure can be viewed at wileyonlinelibrary.com]

in other models, there is a large moisture-flux convergence to the relative north. The magnitude of precipitation for SLPSs is smaller in MERRA-2 than in ERA-I (Figure S4d), which is attributed to a weaker moisture-flux convergence.

5.2 | Mean sea-level pressure and relative vorticity

Here, we would like to understand the simulation of the structure of mean sea-level pressure (MSLP) anomaly and

850 hPa relative vorticity for SLPS composites. Figure 6 shows storm-centred 850 hPa relative vorticity (10^{-5} s^{-1}) in coloured contours and MSLP anomaly in line contours. The difference between composites of MERRA-2 and ERA-I is shown in Figure S4. The maximum relative vorticity and MSLP anomaly are located at the composite centre in all S2S models, the MMM, ERA-I, and MERRA-2. The CMA, NCEP, ECMWF, and ISAC-CNR models simulate the largest relative vorticity and MSLP anomaly, whereas the HMCR (BoM) model simulates the smallest relative vorticity (MSLP anomaly). There is a strong
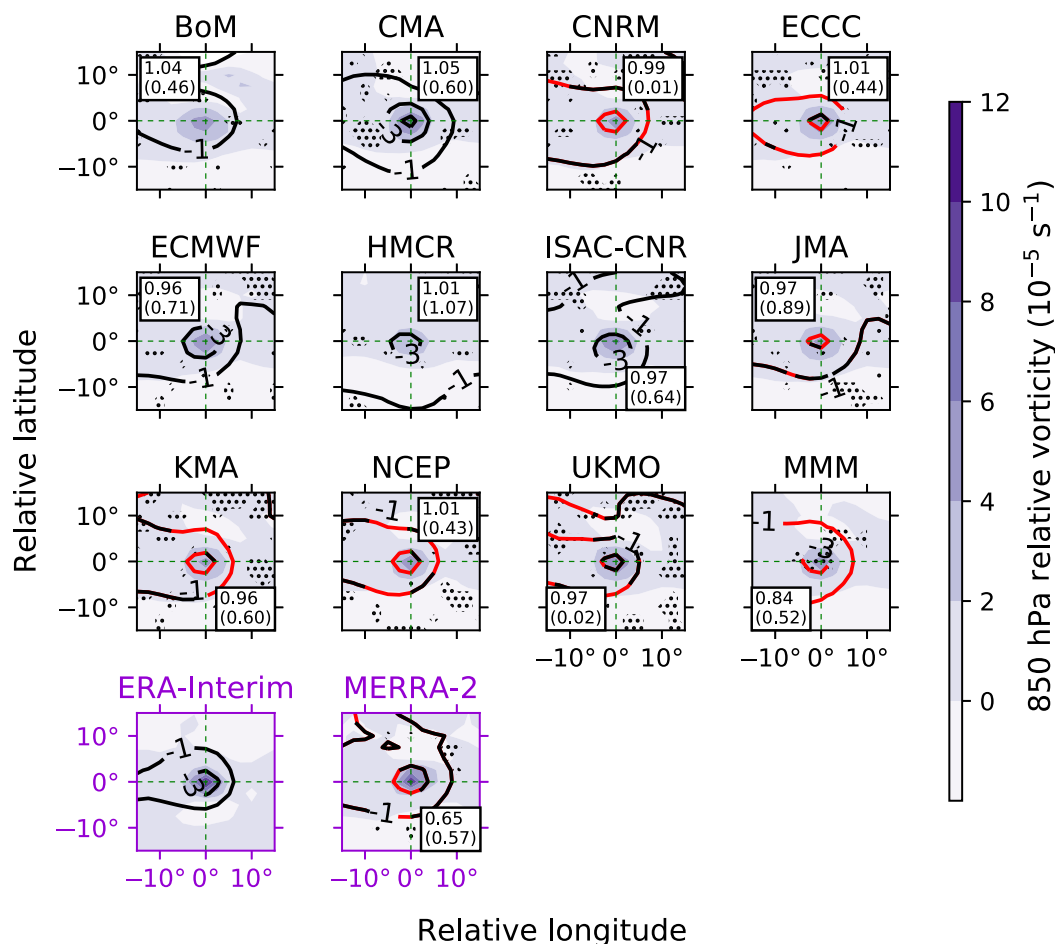
FIGURE 6 Storm-centred relative vorticity (10^{-5} s^{-1}) at 850 hPa in shaded contours and mean sea-level pressure anomaly (hPa) in line contours for composites of strong Indian monsoon low-pressure systems tracked in all ensemble members of 11 subseasonal-to-seasonal (S2S) models and ERA-Interim and Modern-Era Retrospective Analysis for Research and Applications, version 2 (MERRA-2) reanalysis datasets during June–September 1999–2010. The anomaly is considered for forecast lead times of 0–15 days in all S2S models, and is computed against the summer mean climatology for S2S models and ERA-Interim. The multimodel mean (MMM) of S2S models is also shown. Stippling and modified line contours indicate regions where the composite does not significantly differ from ERA-Interim at the 95% level, based on an independent t-test. Numbers indicate the root-mean-square error in the 850 hPa relative vorticity (10^{-5} s^{-1}) and mean sea-level pressure anomaly (hPa, shown in parentheses) between the respective S2S models and ERA-Interim. For MERRA-2, numbers represent root-mean-square error in the same fields, which is computed with respect to ERA-Interim. BoM, Australian Bureau of Meteorology; CMA, China Meteorological Administration; ECCC, Environment and Climate Change Canada; ECMWF, European Centre for Medium-Range Weather Forecasts; HMCR, Hydrometeorological Centre of Russia; ISAC-CNR, Institute of Atmospheric Sciences and Climate of the National Research Council; JMA, Japan Meteorological Agency; KMA, Korea Meteorological Administration; CNRM, Météo-France/Centre National de Recherche Meteorologiques; NCEP, National Centers for Environmental Prediction; UKMO, UK Met Office [Colour figure can be viewed at wileyonlinelibrary.com]

negative and statistically significant (at the 95% confidence level) intermodel linear correlation (Pearson correlation coefficient of −0.74) between maximum MSLP anomaly and maximum precipitation (Figure S6b). The weakest rainfall (Figure 5), therefore, is associated with the weak intensity of SLPSs. The intensity at the composite centre in reanalyses is similar; however, the intensity to the relative north and northeast of the composite centre in MERRA-2 is more than in ERA-I. This does not have any implications for the model result since the spread of errors among models is larger than the observational uncertainty. With respect to ERA-I, the root-mean-square error for MSLP anomaly (850 hPa relative vorticity) is the largest for the HMCR (BoM and CMA) models, whereas the BoM and HMCR models have the largest root-mean-square error for both fields with respect to MERRA-2 (see Table S1).

In conclusion, stakeholders could benefit from the MMM, ECMWF, ISAC-CNR, NCEP, and UKMO models given the best simulation of the horizontal structure of fields discussed in this section.

6 | VERTICAL STRUCTURE

In this section, we analyse the vertical structure of relative vorticity, temperature, and moist static energy of composites of SLPSs in all S2S models, the MMM, ERA-I, and MERRA-2. The vertical structures are drawn above the zero-latitude line, so relative west is to the left and relative east is to the right of 0° relative longitude. Similar to previous analyses, we consider forecast lead times of 0–15 days in all S2S models.

6.1 | Relative vorticity

Figure 7 shows the vertical structure of relative vorticity anomaly of composites of SLPSs in all ensemble members of 11 S2S models, the MMM, ERA-I, and MERRA-2, and Figure S5 shows the difference between MERRA-2 and ERA-I. The structure is zonally symmetric with a tilt towards the relative west, and it has a maximum intensity near the 850 hPa level, which agrees with past studies (e.g.,

Godbole, 1977; Hunt *et al.* 2016a). The BoM and HMCR models simulate the smallest anomalies, whereas models such as the ECMWF and ISAC-CNR simulate the largest anomalies. Compared with ERA-I and MERRA-2, all S2S models and the MMM simulate shallower and weaker anomalies. The overall vorticity structure is shallower in MERRA-2 than in ERA-I. In the MMM, most S2S models, ERA-I, and MERRA-2 there are negative anomalies in the upper troposphere due to the divergent outflow of SLPSs. The root-mean-square error is largest for the HMCR and BoM models with respect to ERA-I and MERRA-2, whereas it is smallest for the ECMWF and CMA models with respect to ERA-I and MERRA-2, respectively. As seen in previous results, the spread in errors among S2S models is larger than the observational uncertainty.

6.2 | Temperature

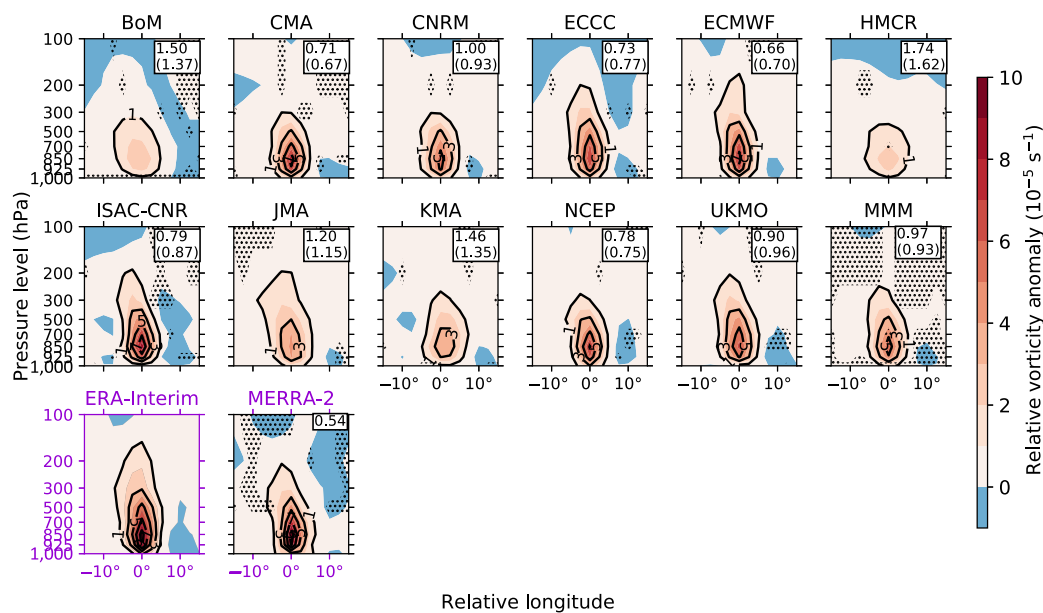We would now like to understand the vertical structure of temperature anomaly (Figure 8). As discussed in Section 1,

FIGURE 7 Vertical structure of relative vorticity anomaly ($10^{-5}\,\mathrm{s}^{-1}$) of storm-centred composites of strong Indian monsoon low-pressure systems in all ensemble members of 11 subseasonal-to-seasonal (S2S) models, ERA-Interim and Modern-Era Retrospective Analysis for Research and Applications, version 2 (MERRA-2) reanalysis datasets during June–September 1999–2010. The anomaly is considered for forecast lead times of 0–15 days in all S2S models, and is computed against the summer mean climatology. The multimodel mean (MMM) of S2S models is also shown. The vertical structure is drawn above the zero-relative-latitude line in a horizontal composite. Stippling indicates regions where the composite does not significantly differ from ERA-Interim at the 95% level, based on an independent *t*-test. Numbers indicate the root-mean-square error in the relative vorticity anomaly ($10^{-5}\,\mathrm{s}^{-1}$) between the respective S2S models and ERA-Interim, or against MERRA-2 in parentheses. The number in MERRA-2 shows the root-mean-square error between MERRA-2 and ERA-Interim. BoM, Australian Bureau of Meteorology; CMA, China Meteorological Administration; ECCC, Environment and Climate Change Canada; ECMWF, European Centre for Medium-Range Weather Forecasts; HMCR, Hydrometeorological Centre of Russia; ISAC-CNR, Institute of Atmospheric Sciences and Climate of the National Research Council; JMA, Japan Meteorological Agency; KMA, Korea Meteorological Administration; CNRM, Météo-France/Centre National de Recherche Meteorologiques; NCEP, National Centers for Environmental Prediction; UKMO, UK Met Office [Colour figure can be viewed at wileyonlinelibrary.com]
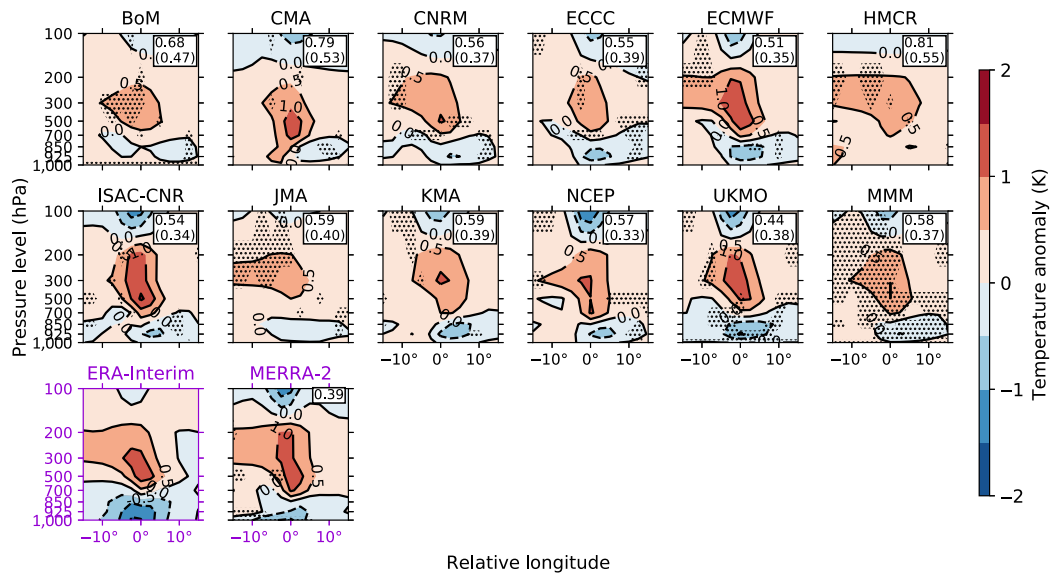
FIGURE 8 As Figure 7, but for temperature anomaly (K). BoM, Australian Bureau of Meteorology; CMA, China Meteorological Administration; ECCC, Environment and Climate Change Canada; ECMWF, European Centre for Medium-Range Weather Forecasts; HMCR, Hydrometeorological Centre of Russia; ISAC-CNR, Institute of Atmospheric Sciences and Climate of the National Research Council; JMA, Japan Meteorological Agency; KMA, Korea Meteorological Administration; CNRM, Météo-France/Centre National de Recherche Meteorologiques; NCEP, National Centers for Environmental Prediction; UKMO, UK Met Office; MERRA-2, Modern-Era Retrospective Analysis for Research and Applications, version 2; MMM, multimodel mean [Colour figure can be viewed at wileyonlinelibrary.com]

LPSs have a warm-over-cold structure; the cold core in the lower troposphere is attributed to evaporative cooling due to precipitation and reduced insolation due to significant cloud cover (Sarker and Chowdhury, 1988; Sørland and Sorteberg, 2015), whereas the warm core is attributed to latent heating from deep convection (Ashok *et al.*, 2000; Hunt *et al.*, 2016b). All S2S models and the MMM simulate the upper-tropospheric warm core; however, there are biases in the simulation of its vertical extent. The composite warm core is shallower in the BoM, ECCC, and JMA models than in other models. It is the weakest in the BoM, JMA, and HMCR models, suggesting that either there is less convection or the convective scheme is producing less heating due to factors such as biases in the vertical moisture flux. The warm core is weaker in the MMM than in reanalyses. In contrast, models such as the ECMWF, ISAC-CNR, UKMO, and NCEP simulate a strong warm core whose magnitude is similar to that in ERA-I and MERRA-2. There is a strong positive and statistically significant (at the 95% confidence level) intermodel linear correlation (Pearson correlation coefficient of 0.74) between the maximum intensity of the warm core at 300 hPa and maximum precipitation within 800 km of the composite centre (Figure S6c).

Unlike for the warm core, there are larger biases in the simulation of the lower-tropospheric cold core. The HMCR model does not simulate the cold core. The most intense structure of the cold core in ERA-I, MERRA-2,

ECCC, ECMWF, and UKMO models is exactly above the composite centre; however, it is displaced in other S2S models and the MMM. Similar to the warm core, the cold core is shallower in the BoM and JMA models than in other models and reanalyses, which is due to the weak intensity of SLPSs. There is a moderate negative and statistically significant (at the 95% confidence level) intermodel linear correlation (Pearson correlation coefficient of −0.61) between the magnitude of the cold core (i.e., maximum 925 hPa temperature anomaly) and maximum precipitation within 800 km of the composite centre (Figure S6d), agreeing with findings of previous studies (Sarker and Chowdhury, 1988; Hunt *et al.*, 2016a) that the development of the cold core is attributed to evaporating precipitation. This result also suggests that the general thermal structure is well captured in models featuring more accurate rainfall (e.g., NCEP). The UKMO model features the smallest root-mean-square error with respect to ERA-I and MERRA-2.

6.3 | Moist static energy

We investigate the vertical structure of moist static energy (MSE) anomaly in this subsection. MSE is a useful thermodynamic parameter to understand moist convection since it is conserved under a hydrostatic balance and moist adiabatic processes. It has been used to analyse LPSs in
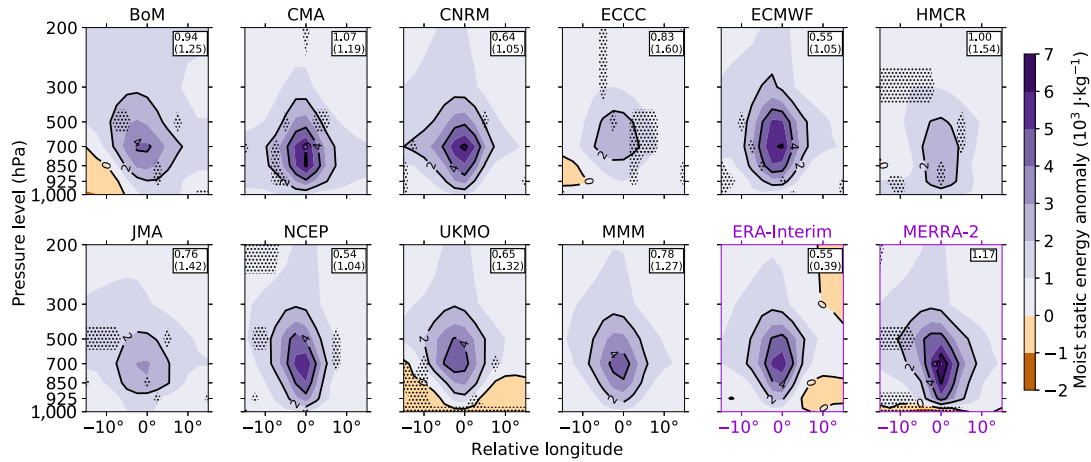
FIGURE 9 As Figure 7, but for moist static energy anomaly (10^3 J·kg^{-1}). The results for the Institute of Atmospheric Sciences and Climate of the National Research Council and Korea Meteorological Administration models are not shown due to the unavailability of the specific humidity field. Output for the 100 hPa level is not shown in ERA-Interim and Modern-Era Retrospective Analysis for Research and Applications, version 2 (MERRA-2) since it is not available in subseasonal-to-seasonal models. BoM, Australian Bureau of Meteorology; CMA, China Meteorological Administration; ECCC, Environment and Climate Change Canada; ECMWF, European Centre for Medium-Range Weather Forecasts; HMCR, Hydrometeorological Centre of Russia; JMA, Japan Meteorological Agency; CNRM, Météo-France/Centre National de Recherche Meteorologiques; NCEP, National Centers for Environmental Prediction; UKMO, UK Met Office; MMM, multimodel mean [Colour figure can be viewed at wileyonlinelibrary.com]

past studies (e.g., Karmakar *et al.*, 2020). The MSE *h* is defined as

$$h = c_{pd}T + q_v L + gz \qquad (4)$$

where c_{pd} is the heat capacity of dry air at constant pressure, T is the temperature, q_v is the specific humidity, L is the latent heat of vaporization of liquid water, g is the acceleration due to gravity, and z is the altitude. We compute the geopotential contribution term gz from the geopotential height. The second term in this equation shows the importance of latent heating and its contribution to the first term that measures the dry-air enthalpy. Therefore, large values of MSE are related to more moisture content, which is associated with the intensity of LPSs. We could not compute MSE anomalies for the ISAC-CNR and KMA models since the specific humidity field is not available. The MSE anomaly in all models, the MMM, ERA-I, and MERRA-2 (Figure 9) is maximum in the lower troposphere near the 850–700 hPa level. This result agrees with Hunt *et al.* (2016a), who inferred that the moisture structure of an MD composite features two maxima: in the upper troposphere and near the 850 hPa level. The MSE anomaly is the weakest in the HMCR, JMA, and ECCC models, which does not exceed 3×10^3 J·kg^{-1}. The ECMWF and CNRM models feature anomalies of 6×10^3 J·kg^{-1}, which are similar to those in MERRA-2. However, the magnitude of the lower-tropospheric MSE anomaly is weaker in MERRA-2 than in ERA-I. Similar to the structure of relative vorticity anomaly (Figure 7) and temperature anomaly (Figure 8), the MSE anomaly structure shows a westward tilt with height in some models, such as BoM and NCEP. The ECMWF and NCEP models feature the smallest root-mean-square error with respect to ERA-I and MERRA-2, whereas the BoM, HMCR, and ECCC models feature large errors.

In conclusion, the ECMWF, NCEP, and UKMO models have the best simulation of horizontal and vertical structures of SLPS composites, whereas the HMCR model has the worst.

7 | VARIABILITY

In order to better represent various LPS processes in models, it is important to understand how the structure evolves with the LPS lifespan as well as forecast lead time of S2S models. Here, we focus on the evolution of 850 hPa relative vorticity, lower-tropospheric cold core, and upper-tropospheric warm core, since they have not been explored in previous studies. We consider these fields at the centre of LPSs. It should be noted that we consider LPSs instead of SLPSs since we are interested in the lifetime evolution of these fields and we would not expect an SLPS to meet its vorticity threshold throughout its life.

7.1 | Evolution over forecast lead time

Understanding how the structure of LPS varies with forecast lead time may provide insights into bias development
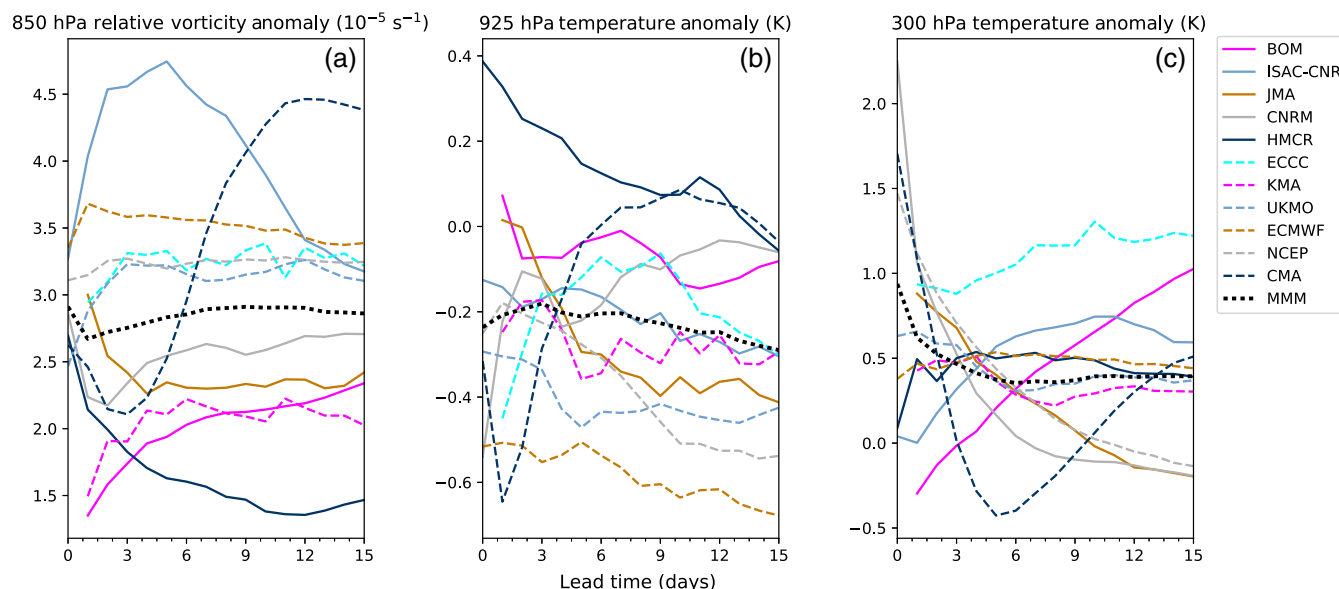
FIGURE 10 (a) Relative vorticity anomaly (10^{-5} s^{-1}) at the 850 hPa level and temperature anomalies (K) at (b) 925 hPa and (c) 300 hPa levels of composites of Indian monsoon low-pressure systems as a function of forecast lead time (days). These anomalies, which are computed against the summer mean climatology, are taken from the centre of low-pressure systems tracked in all ensemble members of 11 subseasonal-to-seasonal models during June–September 1999–2010. The anomalies are considered for forecast lead times of 0–15 days. The multimodel mean (MMM) is also shown. Step 0 is not available for the BoM, ECCC, JMA, and KMA models. BoM, Australian Bureau of Meteorology; CMA, China Meteorological Administration; ECCC, Environment and Climate Change Canada; ECMWF, European Centre for Medium-Range Weather Forecasts; HMCR, Hydrometeorological Centre of Russia; ISAC-CNR, Institute of Atmospheric Sciences and Climate of the National Research Council; JMA, Japan Meteorological Agency; KMA, Korea Meteorological Administration; CNRM, Météo-France/Centre National de Recherche Meteorologiques; NCEP, National Centers for Environmental Prediction; UKMO, UK Met Office [Colour figure can be viewed at wileyonlinelibrary.com]

and how modelled LPS could be better represented in the future. Figure 10 shows the evolution of 850 hPa relative vorticity anomaly, 925 hPa temperature anomaly (a measure of the cold core), and 300 hPa temperature anomaly (a measure of the warm core) for forecast lead times of 0–15 days. In the BoM (HMCR) model, the 850 hPa relative vorticity anomaly increases (decreases) with forecast time, and there is a prominent increase in the relative vorticity anomaly between forecast lead times of 3 and 10 days in the CMA model. The relative vorticity anomaly in the CMA model decreases after attaining the maximum magnitude at forecast lead times of ∼ 5 days. We compute the estimated convective available potential energy (ECAPE; Ditchek *et al.* 2016) to understand the results (not shown). ECAPE is the difference between the surface moist static energy and the upper-tropospheric vertically averaged saturation moist static energy. Ditchek *et al.* (2016) found that ECAPE has the largest anomalous contribution to the seasonal cycle of genesis of MDs. For illustration purposes, we will discuss the results for the CMA and HMCR models. Compared with forecast lead times of 0–5 days, the ECAPE in the CMA model increases by 6×10^3 J·kg^{-1} over the monsoon core zone and head of the BoB during

forecast lead times of 10–15 days. This leads to an increase in the relative vorticity anomaly during forecast lead times of 10–15 days. In contrast, ECAPE difference between forecast lead times of 12–15 days and 0–3 days in the HMCR model is -5×10^3 J·kg^{-1}, suggesting unfavourable conditions for LPSs during forecast lead times of 12–15 days.

Most models feature an intensification of the 925 hPa temperature anomaly with increasing forecast lead times. The intensification of the temperature anomaly in the HMCR model suggests that there is a tendency of more lysis of LPSs with increasing forecast lead times—matured LPSs at longer lead times would have a cooler lower troposphere than their younger counterparts. The CMA model shows anomalous warming in the lower troposphere after ∼ 1 day forecast lead time, suggesting a significant proportion of young LPSs. This is also evident from the 300 hPa temperature anomaly, which shows an increase from lead times of ∼ 6 days onwards. Interestingly, the BoM model also shows anomalous warming at longer lead times at the 300 hPa level, suggesting a significant proportion of young LPSs.

In conclusion, the MMM is less sensitive to forecast lead time than individual S2S models are.
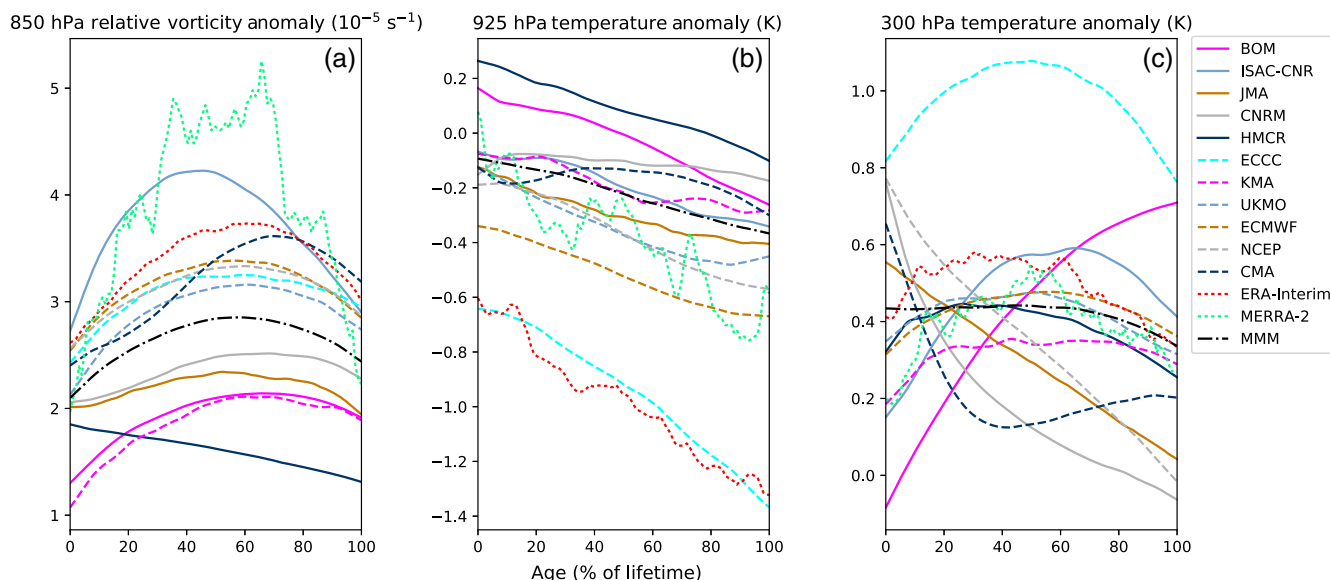
FIGURE 11 (a) Relative vorticity anomaly ($10^{-5}\,\mathrm{s}^{-1}$) at the 850 hPa level and (b, c) temperature anomalies (K) at (b) 925 hPa and (c) 300 hPa levels of composites of Indian monsoon low-pressure systems (LPSs) as a function of LPS lifespan (percentage) during June–September 1999–2010. These anomalies are computed against the summer mean climatology and are considered for forecast lead times of 0–15 days. They are taken from the centre of LPSs tracked in all ensemble members of 11 subseasonal-to-seasonal models and the ERA-Interim and Modern-Era Retrospective Analysis for Research and Applications, version 2 (MERRA-2) reanalysis datasets. The multimodel mean (MMM) is also shown. BoM, Australian Bureau of Meteorology; CMA, China Meteorological Administration; ECCC, Environment and Climate Change Canada; ECMWF, European Centre for Medium-Range Weather Forecasts; HMCR, Hydrometeorological Centre of Russia; ISAC-CNR, Institute of Atmospheric Sciences and Climate of the National Research Council; JMA, Japan Meteorological Agency; KMA, Korea Meteorological Administration; CNRM, Météo-France/Centre National de Recherche Meteorologiques; NCEP, National Centers for Environmental Prediction; UKMO, UK Met Office [Colour figure can be viewed at wileyonlinelibrary.com]

7.2 | Evolution over LPS lifespan

In order to fully compare various LPS processes in S2S models with observed behaviour, it is necessary to study the evolution of structure during LPS lifetime. We interpolate atmospheric fields of interest onto a common time axis, since different LPSs can have a different lifespan. Here, we construct a lifetime-percentage array, following Hunt *et al.* (2016a). We first calculate the percentage age of an LPS at each time step, with the first (final) time step denoting genesis (lysis) or 0% (100%) lifespan, and then interpolate fields for all such time steps on this array. We iterate this process for all LPSs, and finally compute a mean value for each S2S model, ERA-I, and MERRA-2.

Most S2S models along with the MMM feature maximum 850 hPa relative vorticity anomalies around midlife (Figure 11), in agreement with ERA-I, MERRA-2, and previous findings (Hunt *et al.*, 2016a). However, the CMA and HMCR models feature a different pattern. LPSs in the CMA model attain a maximum magnitude at ~70% lifespan, whereas those in the HMCR model do not feature a midlife maximum, suggesting that LPSs do not evolve in a realistic manner. As discussed in the previous subsection, ECAPE in the HMCR model is not favourable

for the intensification or genesis of LPSs at longer lead times, which seems to be preventing LPSs from attaining a midlife maximum. This is supported by findings of Deoras *et al.* (2021a), who found that SLPSs in the HMCR model are not able to propagate inwards over the land (see lysis in figure 4 of that article). The slightly delayed maximum anomaly in the CMA model is attributed to an increase in the relative vorticity during forecast lead times of 3–10 days, when LPSs having genesis in the early period of reforecasts would be in their mature phase. Similar to the findings for relative vorticity anomaly, many models, and ERA-I and MERRA-2 reanalyses, feature a midlife maximum in the 300 hPa temperature anomaly. This is expected, since latent heating due to convection would respond to the LPS intensity. However, BoM shows an increasing temperature anomaly with increasing LPS lifespan, whereas CMA, JMA, and NCEP show a decreasing temperature anomaly. The influence of forecast lead time on these results is clear, since the BoM model features increasing temperature anomalies, whereas the CMA, JMA, and NCEP feature decreasing temperature anomalies with increasing forecast lead time (see Figure 10). The 925 hPa temperature anomalies intensify in all S2S models, ERA-I, and MERRA-2 with increasing LPS lifespan.

More mature LPSs are more likely to be found over land rather than sea. Since land has a lower heat capacity than sea, the effect of reduced insolation due to LPS-cloud cover becomes more prominent over land, resulting in greater cooling in the lower troposphere.

In conclusion, the BoM, CMA, HMCR, and ISAC-CNR models have a high sensitivity to forecast lead time, whereas the MMM has a lower sensitivity than individual models. The evolution of fields with respect to LPS lifespan in the ECWMF, UKMO, and NCEP models, which have the best simulation of horizontal and vertical structures, is most similar to ERA-I and MERRA-2. Therefore, these models and the MMM are useful for understanding LPS processes. The BoM, CMA, HMCR, and ISAC-CNR models, most of which feature large biases in LPS tracks, may be of interest to the modelling community for further exploring the factors responsible for atypical evolution of fields.

8 | CONCLUSIONS

Indian monsoon LPSs are major rain-bearing cyclonic vortices that form during the summer monsoon season (June–September). Despite their important role for water supply and triggering floods, the simulation of their structure by numerical weather prediction models is not well understood. In this article, we analysed the simulation of the structure of SLPSs by 11 models of the Subseasonal-to-Seasonal (S2S) Prediction Project (Vitart *et al.*, 2017). Here, SLPSs are systems whose minimum intensity (central 850 hPa relative vorticity) reaches at least the 75th percentile of the population of all tracked LPSs in the respective S2S model or reanalysis dataset. These systems were analysed in all ensemble members of 11 S2S models during a common reforecast period of June–September 1999–2010 and for forecast lead times of 0–15 days. The results were verified against the ECMWF ERA-I reanalysis and MERRA-2 datasets. The key results of this paper can be summarised as follows.

The simulation of the circulation and summer mean precipitation

All S2S models and the MMM simulated the main features of the lower-tropospheric (850 hPa) monsoon circulation during the climatological period. They also simulated the intensification of the circulation when SLPSs were present. However, there were regional biases in some models, such as BoM, NCEP, and ECCC. We found dry precipitation biases over the monsoon core zone, northeastern India, head of the BoB, and nearby coastal regions in the BoM

and CMA models, which were associated with an easterly wind bias at the 850 hPa level. In contrast, the JMA and ECCC models simulated weak wet biases over the monsoon core zone, which were associated with a westerly wind bias. The precipitation contribution of LPSs to the summer monsoon precipitation was smaller in all S2S models than in ERA-I. This was mainly due to biases in LPS precipitation in most S2S models. In summary, the CMA, ECMWF, HMCR, ISAC-CNR, JMA, KMA, and UKMO models well simulated the monsoon circulation in general, and the MMM outperformed individual models for precipitation.

The simulation of the structure of SLPSs

We examined horizontal structures of precipitation, MSLP, wind, and relative vorticity at 850 hPa for composites of SLPSs. There was a prominent underestimation of maximum precipitation and composite-mean precipitation in the HMCR model, which was associated with the weak intensity of SLPSs. Many models correctly simulated the location of maximum precipitation to the relative southwest of the centre, except for the CMA, ECCC, HMCR, and ISAC-CNR models, which featured a precipitation maximum to the relative south of the centre, coinciding with the maximum moisture-flux convergence at 850 hPa. The CMA, NCEP, ECMWF, and ISAC-CNR (HMCR) models simulated the largest (smallest) relative vorticity and MSLP anomalies.

We found that the vertical structure of relative vorticity anomaly was shallower and weaker in all S2S models and the MMM than in ERA-I and MERRA-2. The upper-tropospheric warm core was shallow (i.e., eroded from the top) in the BoM, ECCC, and JMA models. The HMCR model, which simulated a weak warm core, did not simulate the lower-tropospheric cold core. We also found that the moist static energy anomaly was the weakest in the HMCR, JMA, and ECCC models, and the structure showed a westward tilt with height in some models, such as BoM and NCEP. In summary, the ECMWF, NCEP, and UKMO models had the best simulation of horizontal and vertical structures of SLPSs, whereas HMCR had the worst.

Evolution of fields

We examined the evolution of central 850 hPa relative vorticity and temperature anomalies at 925 hPa and 300 hPa over forecast lead time of S2S models and LPS lifespan. The BoM, CMA, HMCR, and ISAC-CNR models were highly sensitive to forecast lead time due to variations in large-scale conditions, such as the ECAPE (Ditchek *et al.*,

2016). There was an influence of the forecast lead time on the lifetime evolution of fields in these models. However, other S2S models and the MMM featured a midlife maximum in the 850 hPa relative vorticity anomaly and 300 hPa temperature anomaly, in agreement with Hunt *et al.* (2016a). The cold core in the lower troposphere strengthened in all models and the MMM with increasing LPS age. This was due to the effect of reduced insolation due to cloud cover from older LPSs over land. This effect is more prominent over land than sea due to differences in heat capacities.

The results of this paper demonstrate that S2S models simulate the structure of SLPSs, with the ECMWF, NCEP, and UKMO models having the best simulation in general. These results, combined with the results of Deoras *et al.* (2021a), suggest that stakeholders could use S2S models for forecasting LPSs. The results of this study in particular would encourage the modelling community to carry out further investigations of factors such as biases in temperature anomalies in S2S models. In addition, the results would benefit meteorologists and hydrologists, who could use the S2S dataset for developing better products for forecasting SLPSs and their impacts. Since the tropical intraseasonal oscillation (ISO) strongly controls LPS frequency (Krishnamurthy and Ajayamohan, 2010; Deoras *et al.*, 2021b), it is entirely plausible that LPS composites feature more intense structures during active phases of the ISO than during inactive phases. Vitart (2017) found that S2S models can skilfully predict the Madden–Julian Oscillation with a lead time of up to 4 weeks. The S2S models can also predict the Boreal Summer ISO (BSISO)1 and BSISO2 events with a lead time of up to 6–24.5 days and 6.5–14 days, respectively (Jie *et al.*, 2017). However, an analysis of how this affects SLPS structure is beyond the scope of this study. Lastly, a role of the El Niño Southern Oscillation in modulating the frequency and LPS structure needs to be examined in the S2S dataset. In this study, we assumed that any bias in the results due to heterogeneity in the reforecast configuration was insignificant. This aspect could be investigated in a future study by determining the sensitivity of the results to the ensemble size and reforecast frequency. For example, SLPS structures can be intercompared in a range of ensemble members in each S2S model.

AUTHOR CONTRIBUTIONS

A. Deoras: conceptualization; data curation; formal analysis; investigation; methodology; resources; software; validation; visualization; writing – original draft; writing – review and editing. **A. G. Turner:** conceptualization; methodology; supervision; validation; visualization; writing – review and editing. **K. M. R. Hunt:** conceptualization; formal analysis; investigation; methodology; software; supervision; validation; visualization; writing – review and editing.

DATA AVAILABILITY STATEMENT
The track dataset of LPSs identified in S2S models, ERA-I, and MERRA-2 can be accessed at http://doi.org/10.5281/zenodo.4659797. All S2S data used in this study are included in Vitart *et al.* (2017) and are publicly available to the research community from the ECMWF at https://apps.ecmwf.int/datasets/data/s2s-realtime-instantaneous-accum-ecmf/. The ERA-I reanalysis and GPM IMERG datasets are also publicly available at https://apps.ecmwf.int/datasets/data/interim-full-daily/levtype=sfc/ and https://gpm.nasa.gov/data-access/downloads/gpm, respectively.

ORCID
A. Deoras https://orcid.org/0000-0003-1083-9152
A. G. Turner https://orcid.org/0000-0002-0642-6876
K. M. R. Hunt https://orcid.org/0000-0003-1480-3755

REFERENCES
Adames, Á.F. and Ming, Y. (2018) Interactions between water vapor and potential vorticity in synoptic-scale monsoonal disturbances: Moisture vortex instability. *Journal of the Atmospheric Sciences*, 75, 2083–2106. https://doi.org/10.1175/JAS-D-17-0310.1.

Ashok, K., Soman, M. and Satyan, V. (2000) Simulation of monsoon disturbances in a GCM. *Pure and Applied Geophysics*, 157, 1509–1539. https://doi.org/10.1007/PL00001131.

Boos, W., Hurley, J. and Murthy, V. (2015) Adiabatic westward drift of Indian monsoon depressions. *Quarterly Journal of the Royal Meteorological Society*, 141, 1035–1048. https://doi.org/10.1002/qj.2454.

Dee, D.P., Uppala, S.M., Simmons, A.J., Berrisford, P., Poli, P., Kobayashi, S., Andrae, U., Balmaseda, M.A., Balsamo, G., Bauer, P., Bechtold, P., Beljaars, A.C.M., van de Berg, L., Bidlot, J., Bormann, N., Delsol, C., Dragani, R., Fuentes, M., Geer, A.J., Haimberger, L., Healy, S.B., Hersbach, H., Hólm, E.V., Isaksen, L., Kållberg, P., Köhler, M., Matricardi, M., McNally, A.P., Monge-Sanz, B.M., Morcrette, J.-J., Park, B.-K., Peubey, C., de Rosnay, P., C. Tavolato, Thépaut, J.-N. and Vitart, F. (2011) The ERA-Interim reanalysis: Configuration and performance of the

data assimilation system. *Quarterly Journal of the Royal Meteorological Society*, 137, 553–597. https://doi.org/10.1002/qj.828.

Deoras, A., Hunt, K.M.R. and Turner, A.G. (2021a) Comparison of the prediction of Indian monsoon low-pressure systems by subseasonal-to-seasonal prediction models. *Weather and Forecasting*, 36, 859–877. https://doi.org/10.1175/WAF-D-20-0081.1.

Deoras, A., Hunt, K.M.R. and Turner, A.G. (2021b) The four regional varieties of South Asian monsoon low-pressure systems and their modulation by tropical intraseasonal variability. *Weather*, 76, 194–200. https://doi.org/10.1002/wea.3997.

Deoras, A., Hunt, K.M.R. and Turner, A.G. (2021c). *Track dataset of Indian monsoon low-pressure systems in subseasonal-to-seasonal prediction models, ERA-Interim and MERRA-2 reanalysis datasets*. https://doi.org/10.5281/zenodo.4659797.

Ditchek, S.D., Boos, W.R., Camargo, S.J. and Tippett, M.K. (2016) A genesis index for monsoon disturbances. *Journal of Climate*, 29, 5189–5203. https://doi.org/10.1175/JCLI-D-15-0704.1.

Eliot, J. (1884) Account of southwest monsoon storms generated in the Bay of Bengal during 1877–1881. *Memoirs of the India Meteorological Department*, 2, 217–448.

Gelaro, R., McCarty, W., Suárez, M.J., Todling, R., Molod, A., Takacs, L., Randles, C.A., Darmenov, A., Bosilovich, M.G., Reichle, R., Wargan, K., Coy, L., Cullather, R., Draper, C., Akella, S., Buchard, V., Conaty, A., da Silva, A.M., Gu, W., Kim, G.-K., Koster, R., Lucchesi, R., Merkova, D., Nielsen, J.E., Partyka, G., Pawson, S., Putman, W., Rienecker, M., Schubert, S.D., Sienkiewicz, M. and Zhao, B. (2017) The Modern-Era Retrospective Analysis for Research and Applications, version 2 (MERRA-2). *Journal of Climate*, 30, 5419–5454. https://doi.org/10.1175/JCLI-D-16-0758.1.

Godbole, R.V. (1977) The composite structure of the monsoon depression. *Tellus*, 29, 25–40. https://doi.org/10.1111/j.2153-3490.1977.tb00706.x.

Huffman, G.J., Bolvin, D.T., Braithwaite, D., Hsu, K., Joyce, R., Xie, P. and Yoo, S.-H. (2015). *NASA Global Precipitation Measurement (GPM) Integrated Multi-satellite Retrievals for GPM (IMERG)* (Algorithm Theoretical Basis Document (ATBD) Version 4.5). Greenbelt, MD: NASA. https://gpm.nasa.gov/sites/default/files/document_files/IMERG_ATBD_V4.5.pdf.

Hunt, K.M.R. and Fletcher, J.K. (2019) The relationship between Indian monsoon rainfall and low-pressure systems. *Climate Dynamics*, 53, 1859–1871. https://doi.org/10.1007/s00382-019-04744-x.

Hunt, K.M.R. and Menon, A. (2020) The 2018 Kerala floods: A climate change perspective. *Climate Dynamics*, 54, 2433–2446. https://doi.org/10.1007/s00382-020-05123-7.

Hunt, K.M.R. and Parker, D.J. (2016) The movement of Indian monsoon depressions by interaction with image vortices near the Himalayan wall. *Quarterly Journal of the Royal Meteorological Society*, 142, 2224–2229. https://doi.org/10.1002/qj.2812.

Hunt, K.M.R., Turner, A.G., Inness, P.M., Parker, D.E. and Levine, R.C. (2016a) On the structure and dynamics of Indian monsoon depressions. *Monthly Weather Review*, 144, 3391–3416. https://doi.org/10.1175/MWR-D-15-0138.1.

Hunt, K.M.R., Turner, A.G. and Parker, D.E. (2016b) The spatiotemporal structure of precipitation in Indian monsoon depressions. *Quarterly Journal of the Royal Meteorological Society*, 142, 3195–3210. https://doi.org/10.1002/qj.2901.

Hunt, K.M.R., Turner, A.G. and Shaffrey, L.C. (2018) The evolution, seasonality and impacts of western disturbances. *Quarterly Journal of the Royal Meteorological Society*, 144, 278–290. https://doi.org/10.1002/qj.3200.

Hurley, J.V. and Boos, W.R. (2015) A global climatology of monsoon low-pressure systems. *Quarterly Journal of the Royal Meteorological Society*, 141, 1049–1064. https://doi.org/10.1002/qj.2447.

Jie, W., Vitart, F., Wu, T. and Liu, X. (2017) Simulations of the Asian summer monsoon in the sub-seasonal to seasonal prediction project (S2S) database. *Quarterly Journal of the Royal Meteorological Society*, 143, 2282–2295. https://doi.org/10.1002/qj.3085.

Karmakar, N., Boos, W.R. and Misra, V. (2020) Influence of intraseasonal variability on the development of monsoon depressions. *Geophysical Research Letters*, 48. https://doi.org/10.1029/2020GL090425.

Krishnamurthy, V. and Ajayamohan, R. (2010) Composite structure of monsoon low pressure systems and its relation to Indian rainfall. *Journal of Climate*, 23, 4285–4305. https://doi.org/10.1175/2010JCLI2953.1.

Krishnamurti, T., Kanamitsu, M., Godbole, R., Chang, C.-B., Carr, F. and Chow, J.H. (1975) Study of a monsoon depression (I): Synoptic structure. *Journal of the Meteorological Society of Japan. Series II*, 53, 227–240. https://doi.org/10.2151/jmsj1965.53.4_227.

Krishnamurti, T., Kanamitsu, M., Godbole, R., Chang, C.-B., Carr, F. and Chow, J.H. (1976) Study of a monsoon depression (II), dynamical structure. *Journal of the Meteorological Society of Japan. Series II*, 54, 208–225. https://doi.org/10.2151/jmsj1965.54.4_208.

Lee, C.-Y., Camargo, S.J., Vitart, F., Sobel, A.H. and Tippett, M.K. (2018) Subseasonal tropical cyclone genesis prediction and MJO in the S2S dataset. *Weather and Forecasting*, 33, 967–988. https://doi.org/10.1175/WAF-D-17-0165.1.

Liu, Z. (2016) Comparison of Integrated Multisatellite Retrievals for GPM (IMERG) and TRMM Multisatellite Precipitation Analysis (TMPA) monthly precipitation products: Initial results. *Journal of Hydrometeorology*, 17, 777–790. https://doi.org/10.1175/JHM-D-15-0068.1.

Mishra, K., Sharma, M. and Mohapatra, M. (2021) Performance of numerical weather prediction models in predicting track of recurving cyclone Vayu over Arabian Sea during June 2019. *Journal of Earth System Science*, 130, 25. https://doi.org/10.1007/s12040-020-01533-7.

Mooley, D.A. (1973) Some aspects of Indian monsoon depressions and the associated rainfall. *Monthly Weather Review*, 101, 271–280. https://doi.org/10.1175/1520-0493(1973)101<0271:SAOIMD>2.3.CO;2.

Mulky, G. and Banerji, A. (1960) The mean upper-wind circulation around monsoon depressions in India. *Journal of Atmospheric Sciences*, 17, 8–14. https://doi.org/10.1175/1520-0469(1960)017<0008:TMUWCA>2.0.CO;2.

Murthy, V.S. and Boos, W.R. (2020) Quasigeostrophic controls on precipitating ascent in monsoon depressions. *Journal of the Atmospheric Sciences*, 77, 1213–1232. https://doi.org/10.1175/JAS-D-19-0202.1.

Pisharoty, P. and Asnani, G. (1957) Rainfall around monsoon depressions over India. *Indian Journal Meteorology and Geophysics*, 8, 15–20.

Prakash, S., Mitra, A.K., AghaKouchak, A., Liu, Z., Norouzi, H. and Pai, D. (2018) A preliminary assessment of GPM-based multi-satellite precipitation estimates over a monsoon dominated

region. *Journal of Hydrology*, 556, 865–876. https://doi.org/10.1016/j.jhydrol.2016.01.029.

Prakash, S., Mitra, A.K., Pai, D. and AghaKouchak, A. (2016) From TRMM to GPM: How well can heavy rainfall be detected from space?. *Advances in Water Resources*, 88, 1–7. https://doi.org/10.1016/j.advwatres.2015.11.008.

Praveen, V., Sandeep, S. and Ajayamohan, R. (2015) On the relationship between mean monsoon precipitation and low pressure systems in climate model simulations. *Journal of Climate*, 28, 5305–5324. https://doi.org/10.1175/JCLI-D-14-00415.1.

Rajamani, S. and Rao, K.V. (1981) On the occurrence of rainfall over southwest sector of monsoon depression. *MAUSAM*, 32, 215–220. https://doi.org/10.54302/mausam.v32i3.3367.

Rajeevan, M., Gadgil, S. and Bhate, J. (2010) Active and break spells of the Indian summer monsoon. *Journal of Earth System Science*, 119, 229–247. https://doi.org/10.1007/s12040-010-0019-4.

Saha, K., Sanders, F. and Shukla, J. (1981) Westward propagating predecessors of monsoon depressions. *Monthly Weather Review*, 109, 330–343. https://doi.org/10.1175/1520-0493(1981)109<0330:WPPOMD>2.0.CO;2.

Sanders, F. (1984) Quasi-geostrophic diagnosis of the monsoon depression of 5–8 July 1979. *Journal of Atmospheric Sciences*, 41, 538–552. https://doi.org/10.1175/1520-0469(1984)041%3C0538:QGDOTM%3E2.0.CO;2.

Sarker, R. and Chowdhury, A. (1988) A diagnostic structure of monsoon depressions. *MAUSAM*, 39, 9–18. https://doi.org/10.54302/mausam.v39i1.3173.

Sikka, D.R. (1978). Some aspects of the life history, structure and movement of monsoon depressions. In T. N. Krishnamurti (Ed.), *Monsoon dynamics* (pp. 1501–1529). Basel, Switzerland: Birkhäuser. https://doi.org/10.1007/978-3-0348-5759-8_21.

Snedecor, G.W. and Cochran, W.G. (1989) *Statistical methods* (8th ed.). Ames, IA: Iowa State University Press.

Sørland, S.L. and Sorteberg, A. (2015) The dynamic and thermodynamic structure of monsoon low-pressure systems during extreme rainfall events. *Tellus A: Dynamic Meteorology and Oceanography*, 67, 27039. https://doi.org/10.3402/tellusa.v67.27039.

Sperber, K., Annamalai, H., Kang, I.-S., Kitoh, A., Moise, A., Turner, A., Wang, B. and Zhou, T. (2013) The Asian summer monsoon: An intercomparison of CMIP5 vs. CMIP3 simulations of the late 20th century. *Climate Dynamics*, 41, 2711–2744. https://doi.org/10.1007/s00382-012-1607-6.

Stano, G., Krishnamurti, T., Vijaya Kumar, T. and Chakrabory, A. (2002) Hydrometeor structure of a composite monsoon depression using the TRMM radar. *Tellus A: Dynamic Meteorology and Oceanography*, 54, 370–381. https://doi.org/10.3402/tellusa.v54i4.12154.

Vitart, F. (2017) Madden–Julian Oscillation prediction and teleconnections in the S2S database. *Quarterly Journal of the Royal Meteorological Society*, 143, 2210–2220. https://doi.org/10.1002/qj.3079.

Vitart, F., Ardilouze, C., Bonet, A., Brookshaw, A., Chen, M., Codorean, C., Déqué, M., Ferranti, L., Fucile, E., Fuentes, M., Hendon, H., Hodgson, J., Kang, H.-S., Kumar, A., Lin, H., Liu, G., Liu, X., Malguzzi, P., Mallas, P.I., Manoussakis, M., Mastrangelo, D., MacLachlan, C., McLean, P., Minami, A., Mladek, R., Nakazawa, T., Najm, S., Nie, Y., Rixen, M., Robertson, A.W., Ruti, P., Sun, C., Takaya, Y., Tolstykh, M., Venuti, F., Waliser, D., Woolnough, S., Wu, T., Won, D.-J., Xiao, H., Zaripov, R. and Zhang, L. (2017) The Subseasonal to Seasonal (S2S) Prediction Project database. *Bulletin of the American Meteorological Society*, 98, 163–173. https://doi.org/10.1175/BAMS-D-16-0017.1.

Yoon, J.H. and Chen, T.C. (2005) Water vapor budget of the Indian monsoon depression. *Tellus A: Dynamic Meteorology and Oceanography*, 57, 770–782. https://doi.org/10.3402/tellusa.v57i5.14737.

SUPPORTING INFORMATION

Additional supporting information can be found online in the Supporting Information section at the end of this article.

How to cite this article: Deoras, A., Turner, A.G. & Hunt, K.M.R. (2022) The structure of strong Indian monsoon low-pressure systems in subseasonal-to-seasonal prediction models. *Quarterly Journal of the Royal Meteorological Society*, 1–20. Available from: https://doi.org/10.1002/qj.4296